Research Square

Preprints are preliminary reports that have not undergone peer review.
They should not be considered conclusive, used to inform clinical practice,
or referenced by the media as validated information.

Unifying Mechanics and Surgery for Analytical Total Knee Arthroplasty

Da Lu
Beijing Jishuitan Hospital, Capital Medical University
Haotian Zhang
Beijing Jishuitan Hospital, Capital Medical University
Guangmin Yang
Beijing Jishuitan Hospital, Capital Medical University
Hanlong Zheng
Beijing Jishuitan Hospital, Capital Medical University
Zheqi Fan
Beijing Jishuitan Hospital, Capital Medical University
Ka Chun Thomas Leung
Queen Mary Hospital & Duchess of Kent Children's Hospital
Zhaolun Wang
Beijing Jishuitan Hospital, Capital Medical University
Zhenghang She
Beijing Jishuitan Hospital, Capital Medical University
Linyi Zhang
Beijing National Day School
Dejin Yang
Beijing Jishuitan Hospital, Capital Medical University
Yixin Zhou
orthoyixin@yahoo.com

Beijing Jishuitan Hospital, Capital Medical University

Article

Keywords:

Posted Date: November 24th, 2026

DOI: https://doi.org/10.21203/rs.3.rs-11697362/v1

License: This work is licensed under a Creative Commons Attribution 4.0 International License.
Read Full License

Additional Declarations: Competing interest reported. Y.Z. is a named inventor on a patent application related to the TKA Balance Solver described in this manuscript. The remaining authors declare no competing interests.

Unifying Mechanics and Surgery for Analytical Total Knee Arthroplasty

Author Information

Affiliations

[1]Department of Orthopaedic Surgery, Beijing Jishuitan Hospital, Capital Medical University, 100035, Beijing, China

[2]Beijing Research Institute of Traumatology and Orthopaedics, 100035, Beijing, China

[3]Queen Mary Hospital & Duchess of Kent Children's Hospital, Pokfulam, Hong Kong SAR, China

[4]Beijing National Day School, 100039, Beijing, China

Da Lu[1,2], Haotian Zhang[1,2], Guangmin Yang[1,2], Hanlong Zheng[1,2], Zheqi Fan[1], Ka Chun Thomas Leung[3], Zhaolun Wang[1,2], Zhenghang She[1], Linyi Zhang[4], Dejin Yang[1,2] & Yixin Zhou[1,2]

Contributions

Y.Z. led the overall conceptualization and supervision of the study and contributed to visualization, funding acquisition, project administration, and writing – review & editing. D.L. contributed to conceptualization, methodology, investigation, visualization, funding acquisition, project administration, supervision, writing – original draft, and writing – review & editing. D.Y. led the conceptualization and supervision of the study and contributed to writing – review & editing. G.Y., H.L.Z., K.C.T.L., and Z.W. contributed to writing – review & editing. H.T.Z., and Z.F. contributed to methodology, clinical follow-up and data processing. Z.S. and L.Z. contributed to data processing and investigation.

Corresponding author

Correspondence to: Dejin Yang (fafnirdj@163.com) & Yixin Zhou (orthoyixin@yahoo.com)

Abstract

Despite advances in surgical philosophies and technologies, total knee arthroplasty (TKA) leaves 15–20% of patients dissatisfied. Here, we report an analytical framework unifying robotic surgery, intraoperative soft-tissue mapping, and kinematic tracking to optimize TKA. Using a novel dynamic tensioner, we captured patient-specific soft-tissue elasticity. To elucidate the underlying mechanics, we formulated a Kinematic Conflict Equation (KCE) revealing the intrinsic interplay among soft-tissue constraints, component positioning, and implant geometry. Through dimensional reduction, we derived a clinically actionable Kinematic Pattern Equation (KPE) that distills these interactions into specific metrics. In a 356-knee cohort, we identified an extension-state metric ($S \approx 1.3$) serving as a threshold to trigger soft-tissue release. During flexion, a metric reflecting posterior tethering force (Q) elucidated a kinematic transition band ($Q \approx 0.35–0.45$) governing tibiofemoral rollback. Crucially, outcome analyses revealed that guiding intraoperative Q into a defined therapeutic window ($0.28 \leq Q \leq 0.40$) directly translates to superior functional recovery. By bridging mechanics and surgery, this parameter-driven approach enables individualized optimization, transforming TKA from an empirical practice into a rigorous analytical procedure.

Introduction

Total knee arthroplasty is the standard surgical treatment for end-stage knee osteoarthritis, resurfacing the damaged cartilage to relieve pain and restore joint function (Fig. 1a). The demand for primary total knee arthroplasty (TKA) in the United States is projected to reach 3.48 million procedures annually by 2030[1]. Even with recent advances in alignment philosophies, implant

design, navigation, and robotics, improvements in functional outcomes and patient satisfaction have largely plateaued[2-4]. Successful TKA hinges on biomechanical optimization—harmonizing limb alignment, component positioning, and implant geometry with the surrounding soft-tissue envelope[5-7]. However, contemporary TKA struggles to achieve this delicate harmony, as fixed implant geometry and predetermined bone-cutting protocols frequently clash with native soft-tissue constraints.

In current TKA practice, because implant geometry is fixed and bone cuts cannot be easily fine-tuned intraoperatively, releasing surrounding soft tissues remains the primary method to restore knee balance and kinematics[8]. However, this invasive release procedure typically relies on the surgeon's subjective assessment of tissue tension and gap symmetry without a quantitative target[9,10], resulting in questionable controllability and reproducibility[11]. While robotic-assisted TKA has substantially improved the accuracy and reproducibility of bone resection and gap measurement[12-15] (Fig. 1b,c), existing robotic systems still lack the ability to quantitatively evaluate soft-tissue elastic behavior and optimize surgical planning accordingly[16] .

At the core of this limitation lies kinematic conflict—the discrepancy between the motion imposed by the implant's articular geometry and that guided by the patient's native soft-tissues. Because component positioning, implant geometry, and soft-tissue constraints are highly interdependent, modifying any of these parameters in isolation fails to effectively resolve this conflict—the root cause of mechanical failures following TKA, including joint instability, stiffness, polyethylene wear, and implant loosening.

To resolve this conflict, we developed a novel soft-tissue tensioner[17] (the TKA Solver) to dynamically characterize soft-tissue elasticity and quantify joint gap behavior during TKA (Fig.

1d,e), generating intraoperative force–gap matrices at different flexion angles (Fig. 1f). By integrating these objective soft-tissue metrics with component positioning and implant geometry, we framed TKA as a patient-specific optimization problem (Fig. 1g). Through theoretical derivation based on Lagrangian and Newtonian mechanics, we formulated the Kinematic Conflict Equation (KCE) and the Kinematic Pattern Equation (KPE). Applying these theoretical models to our intraoperative measurements enables us to mathematically predict and achieve biomechanically optimized, low-conflict kinematic states—a capability we further validated against postoperative functional outcomes. Ultimately, this framework introduces "Analytical TKA", providing a unified, fully quantitative approach to seamlessly integrate underlying biomechanics with surgical practice.

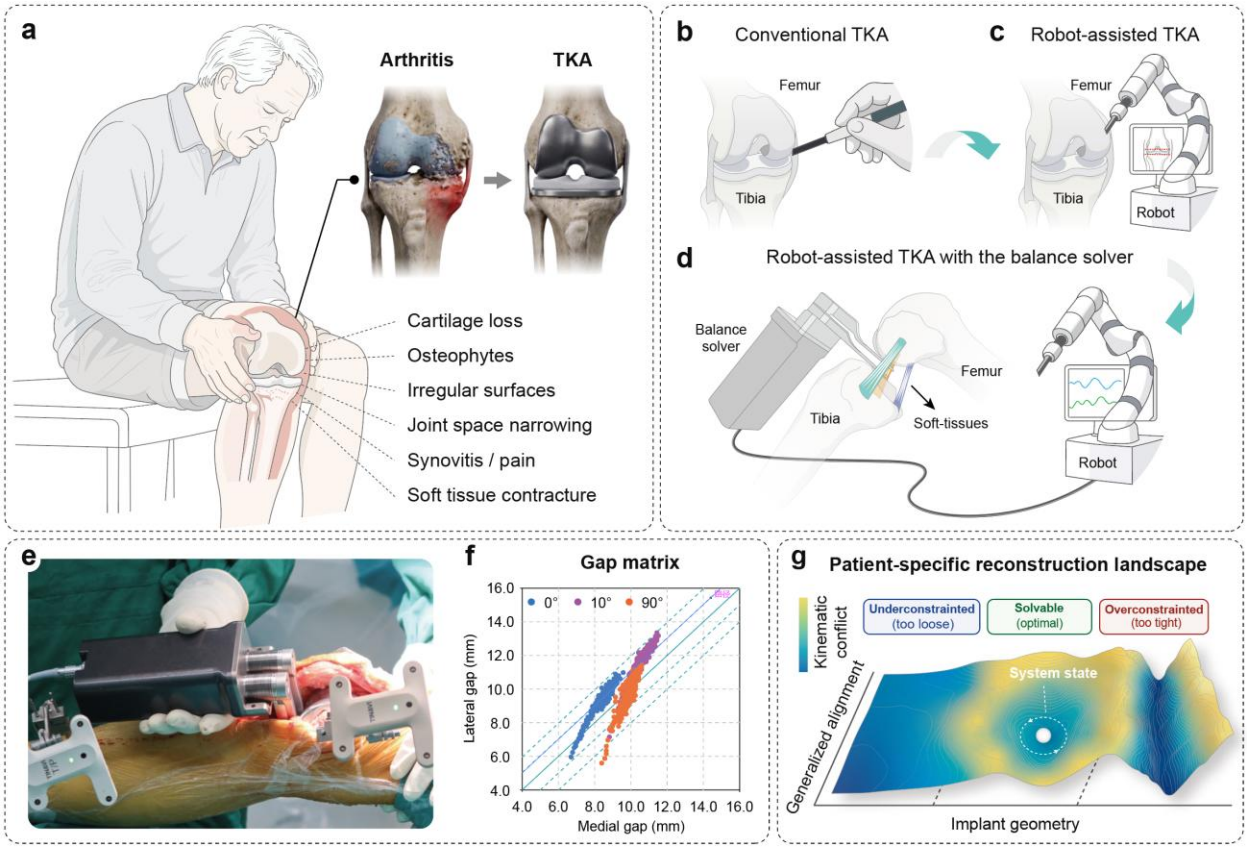


Fig. 1 | Soft tissue solver for measuring soft tissue tension during total knee arthroplasty (TKA) surgery. a, Schematic illustration of an advanced knee osteoarthritis (KOA) patient who needs TKA. In severe KOA patients, the knee joint typically presents with pain, limb deformity, and contracture due to cartilage loss and an imbalance in soft-tissue tension. **b**, **c** Currently, the resection of the lesion area and the implantation of the prosthesis are typically performed manually (**b**) or with robotic assistance (**c**). **d**, Schematic of the intraoperative application of the balance solver. **e**, Representative intraoperative photograph showing application of the balance solver during TKA. **f**, Representative gap matrix showing paired medial and lateral compartment gaps measured under progressive loading at 0°, 10° and 90° of knee flexion. **g**, Conceptual representation of the patient-specific reconstruction space constructed by implant alignment, implant geometry, and soft-tissue constraints. The landscape illustrates how different combinations of surgical variables correspond to under-constrained, solvable, and over-constrained states.

Results

Design and characterization of the TKA Solver

Conventional instruments in TKA, such as static spacer blocks and sensor-embedded trials, act merely as passive gauges that capture discrete snapshots of joint gaps or localized contact forces. They fail to delineate the continuous soft-tissue compliance. To overcome these limitations, we developed a novel dynamic tensioning device: the “TKA Solver” (Fig. 2a). Driven by a vertical lifting motor, its two independent spreading actuators enable precise, continuous force-displacement mapping. A medial preload was combined with repeated lateral load sweeps (Fig. 2b,c). Before clinical implementation, in vitro testing confirmed its mechanical fidelity (Fig. 2d). The device demonstrated high stability across its operating range, with average measurement

errors tightly constrained to 0.44 N for force, 0.14 mm for displacement, and 0.41° for angular deviation. This stringent error control ensures that subsequent intraoperative measurements reliably reflect the true elastic behavior of the native ligaments without instrumental artifacts.

Instead of relying on a singular, empirically chosen tension, the Solver executes a systematic load-sweeping protocol (30 N to 100 N in 5 N increments) independently across the medial and lateral compartments. This asymmetric loading methodology generates a continuous gap-tension matrix whose geometric distribution directly correlates with surgical parameters. Specifically, the spatial position of the matrix relative to the 45-degree diagonal reflects gap symmetry and absolute gap size, which are intrinsically dictated by the implemented bone resection. Concurrently, the morphological profile of the matrix—such as the matrix slope at full extension (*S*)—characterizes the intrinsic properties of the periarticular soft tissue, serving as a quantitative determinant for the necessity and extent of soft-tissue release.

During robotic-assisted TKA, the Solver was positioned at 0°, 10° and 90° of flexion (Fig. 2e), generating angle-specific gap matrices that capture the soft-tissue response across these flexion states (Fig. 2f, g). For instance, intraoperative recordings at 90° typically exhibited a steeper slope compared to 0° and 10° (Fig. 2f), effectively quantifying physiological lateral laxity in deep flexion. By transforming subjective “tissue feel” into a high-fidelity mechanical dataset, the device transcends simple measurement; it provides concurrent, data-driven guidance to define the patient-specific biomechanical solution space (Fig. 1g) and optimize both resection parameters and soft-tissue balancing. In parallel, robotic tracking of tibiofemoral motion enabled reconstruction of the femoral condylar contact-point trajectories (Fig. 2h). Representative trajectories illustrated patterns without a clear medial-pivot configuration (Fig. 2i) and with relatively greater lateral than medial excursion, consistent with medial-pivot behavior (Fig. 2j).

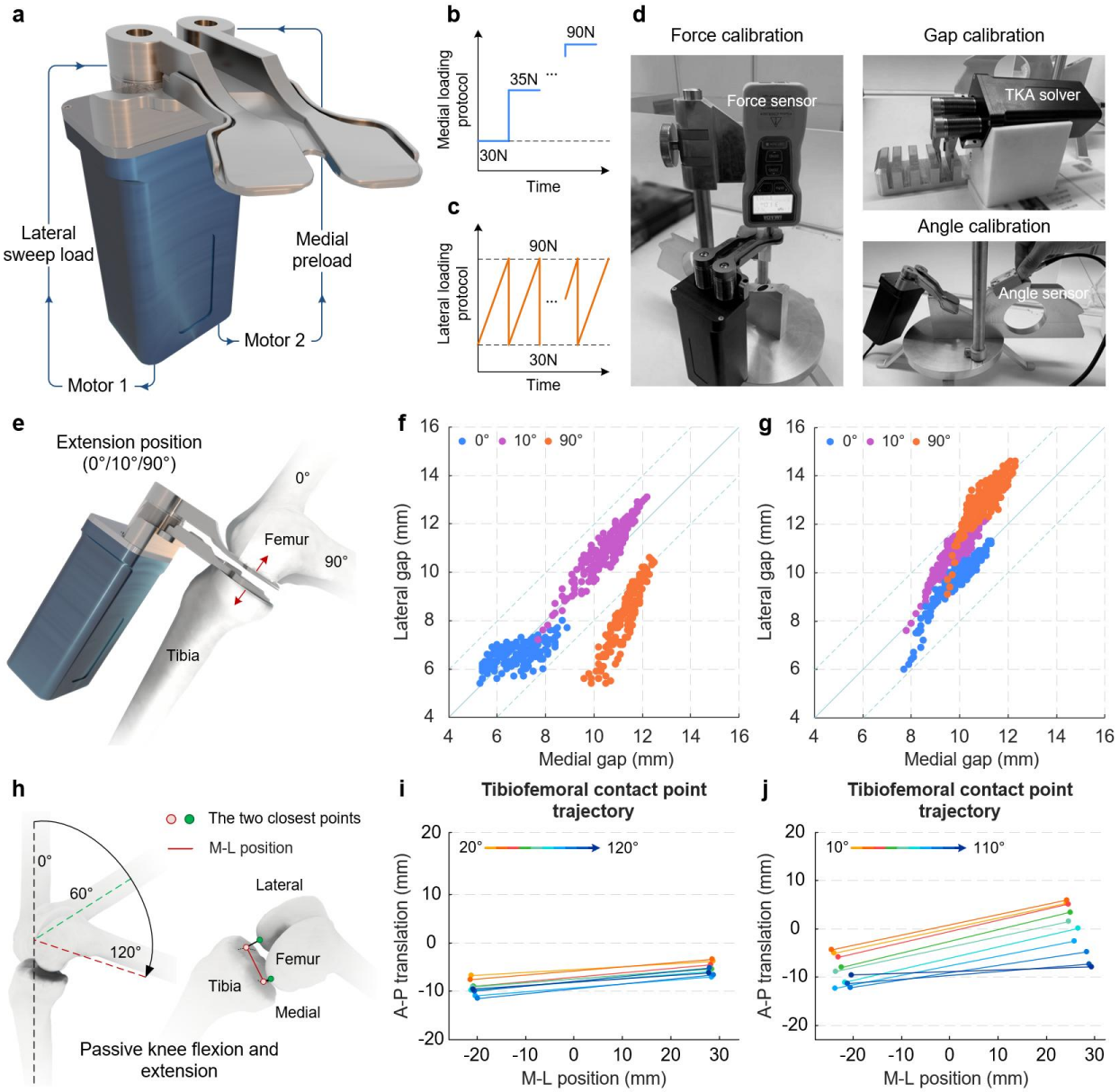


Fig. 2 | Solver calibration, force–gap measurements and tibiofemoral kinematic tracking. a, Schematic design of the balance solver. The device comprises two independently driven spreading arms and a connected vertical lifting mechanism. One side provides medial preload, and the other applies a lateral sweep load, enabling controlled opening of the tibiofemoral space. **b**, Medial loading protocol. The medial side was preloaded from 30 N and then increased stepwise to the target load. **c**, Lateral loading protocol. Under each medial preload condition, the lateral side was swept repeatedly from 30 N to 100 N to generate a series of compartmental gap

responses. **d**, *In vitro* calibration of the balance solver. **e**, Intraoperative application. After the initial bone cuts, the medial and lateral paddles are inserted into the joint space for measurements at defined flexion angles (0°, 10°, and 90°). **f,g**, Representative gap matrices obtained during intraoperative loading. Each point represents one paired measurement of medial and lateral gap under a specific loading condition. (**f)** shows a representative matrix with a steeper 90° relationship and relatively smaller medial gap values than lateral gap values, whereas (**g)** shows a representative matrix with more nearly matched medial and lateral opening across flexion states. **h**, The tibiofemoral contact point is defined as the projection of the lowest point of the femoral condyle onto the tibial plateau. **i,j**, Representative condylar-trajectory patterns during knee flexion, with colors representing specific flexion angles. (**i)** displays a trajectory with similar medial and lateral femoral rollback, whereas (**j**) exhibits a typical medial-pivot pattern, characterized by restricted medial translation and pronounced lateral excursion.

A Lagrangian and Newtonian framework for analytical knee reconstruction

The Solver enables the precise calibration of the patient-specific soft-tissue elasticity profile, while the robotic system transforms bone resection into a highly granular and continuously tunable variable. The convergence of these two technological capabilities allows us to reframe TKA as a constrained biomechanical optimization problem with a mathematically determinable optimal solution. Applying the principles of Lagrangian mechanics, we derived the Kinematic Conflict Equation (KCE) to mathematically decouple and formalize the complex interactions among soft-tissue constraints, component positioning, and implant geometry (Fig. 3a).

$$\frac{\partial^2 u}{\partial a^2} + k\frac{\partial^2 u}{\partial g^2} = f \tag{1}$$

In this formulation, u represents the kinematic-conflict displacement field that quantifies the biomechanical mismatch. The variable (a) denotes the generalized alignment (encompassing limb alignment and implant positioning), (g) represents the implant geometry, and (k) specifies the patient's native soft-tissue constraint state objectively derived from the Solver. The term (f) accounts for the generalized external forces such as loads a knee sustains.

In conventional TKA, implant geometry (g) is fixed, and bone resections (a) offer limited intraoperative flexibility. Consequently, surgeons are forced to achieve joint balance by physically altering the native constraint state (k) through soft-tissue releases with unpredictable, and potentially detrimental, kinematic consequences. While contemporary robotic systems transform alignment (a) into a continuously tunable variable, it remains unclear how to optimally adjust this parameter without a quantitative soft-tissue target. The KCE paradigm resolves this dilemma by treating the patient's native soft-tissue elasticity (k) as a fundamental and measurable boundary condition. By analytically coupling the surgical variables (a and g) under this defined constraint, the KCE delineates a multidimensional stability topography—a landscape that explicitly maps the mechanically compatible and stable kinematic zones for the reconstructed knee (Fig. 3b–d).

The KCE demonstrates that both insufficient and excessive soft-tissue constraints (k) inevitably exacerbate kinematic conflict. As illustrated in the simulated landscapes (Fig. 3b–d), under insufficient constraints, the stability topography is excessively flat; it lacks the necessary energy walls to restrain aberrant kinematics, a state mathematically corresponding to joint instability. Conversely, excessive constraints drastically shrink the stability region, creating a rigid system where even physiological motion incurs a severe energy penalty, effectively modeling the biomechanics of joint stiffness.

Critically, at an optimal constraint level, the topography forms a distinct energy valley. The floor of this valley defines the optimal kinematic trajectory, permitting stability in motion. Any deviation from this path encounters steep energy walls, which act as restoring forces that push the joint back toward its stable trajectory. Within this well-constrained landscape, alignment (a) and implant geometry (g) serve as the navigational parameters. The essence of robotic surgical optimization, therefore, is to systematically tune a and g to maneuver the reconstructed joint into the global minimum of this energy valley.

By formalizing three distinct mechanical states—under-constrained, well-constrained, and over-constrained—the KCE establishes a rigorous theoretical boundary for surgical intervention. Soft-tissue release (which physically alters the boundary parameter k) is mathematically justified if and only if the native constraints are inherently excessive. This over-constrained state creates a prohibitively steep energy valley where tuning a and g alone is insufficient to resolve the severe conflict penalty. Complete mathematical derivations and stability conditions are provided in the Supplementary Information A1-A3.

While the KCE governs the global energetic stability by mathematically coupling soft-tissue constraints (k), alignment (a), and implant geometry (g), this high-dimensional topographical landscape remains unobservable during surgery. To bridge the gap between theoretical system formulation and actionable surgical targets, we reduced the dimensionality of the KCE to establish the Kinematic Pattern Equation (KPE).

$$R = \mathrm{F}\left[S(\theta), Q(\theta); \boldsymbol{\gamma}(a, g)\right]$$

To model the complex intraoperative soft-tissue constraints, the KPE leverages two actionable metrics extracted from the intrinsic Solver data: *S* (the medial-to-lateral constraint ratio) and *Q* (the posterior-to-medial constraint ratio) (Fig. 3e).

S and *Q* play distinct, hierarchical roles. *S* acts as the structural foundation, defining the permissible kinematic envelope of the system. Within this boundary, *Q* serves as the primary modulator, driving the knee across distinct kinematic phases—from paradoxical anterior sliding to a near-physiological medial-pivot rollback. As *S* increases (indicating severe medial-lateral asymmetry), the permissible range for *Q* drastically narrows (Fig. 3f), rendering the joint hyper-sensitive to posterior tension. Conversely, maintaining *S* within an optimal range allows *Q* to safely maneuver the joint into a stable medial-pivot trajectory.

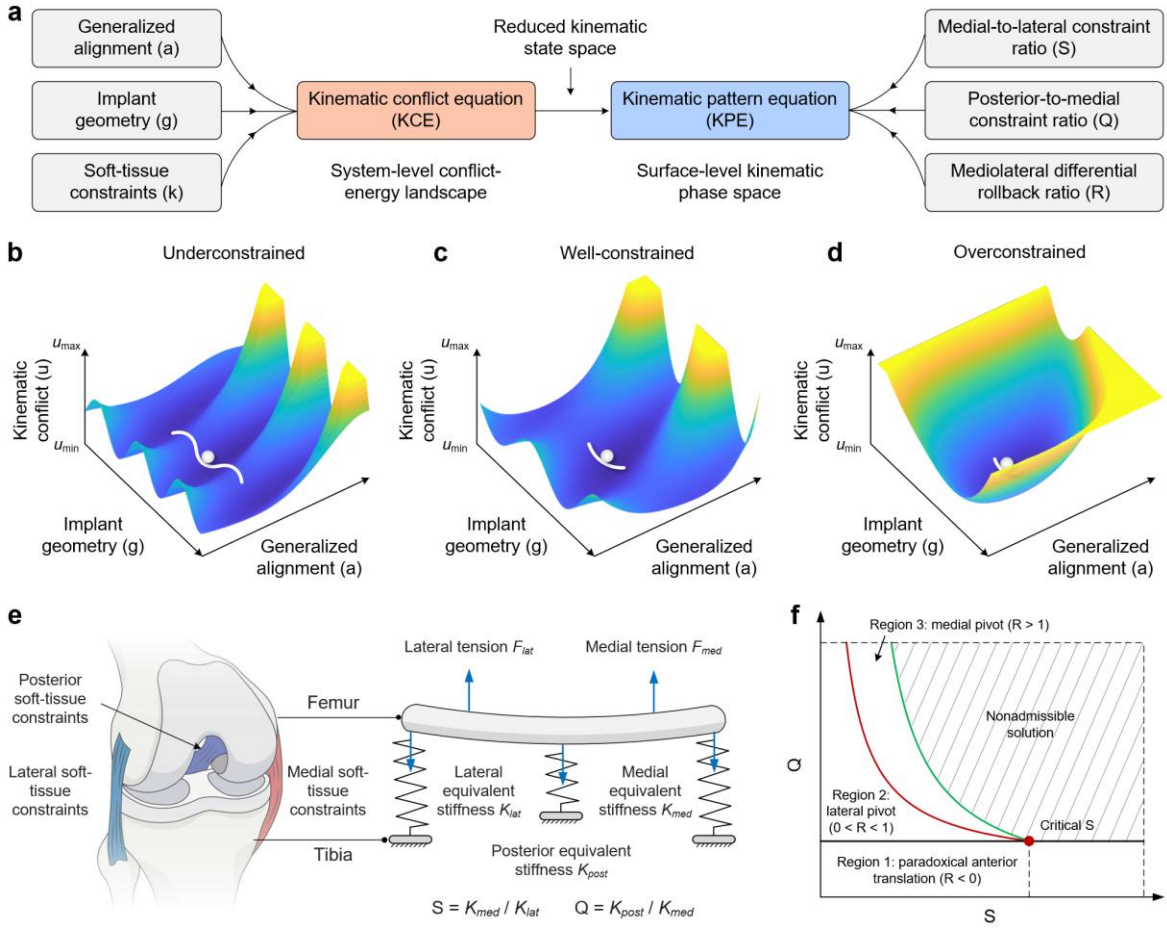


Fig. 3 | Kinematic Conflict Equation (KCE) and kinematic pattern equation (KPE) relating reconstruction variables to soft-tissue constraints and the tibiofemoral kinematics. a, The KCE integrates generalized alignment (a), implant geometry (g), and the patient-specific soft-tissue constraint state (k) to describe system-level kinematic conflict. Dimensional reduction at the tibiofemoral interface yields the KPE, in which the extension-state metric S, flexion-state metric Q, and differential rollback ratio R provide reduced coordinates for describing constraint state and kinematic pattern. **b-d**, Representative KCE-derived kinematic-conflict landscapes generated for increasing levels of soft-tissue constraints. The horizontal axes represent generalized alignment (a) and implant geometry (g), and the surface height and color represent the magnitude of kinematic conflict (u). Under-constrained systems (**b**) exhibit a broad, weakly confined low-conflict region; an intermediate constraint state (**c**) produces a defined low-conflict region while retaining tolerance to changes in alignment and implant geometry; and over-constrained systems (**d**) exhibit a narrower admissible region. The white marker and trajectory illustrate the possible location and local evolution of the system state within each landscape. **e**, Mechanical representation of the reduced soft-tissue constraint variables used in the KPE. Medial and lateral soft-tissue constraints are represented by effective stiffnesses, K_{med} and K_{lat}, and the effective posterior constraint is represented by K_{post}. The extension-state metric is defined as $S = K_{med} / K_{lat}$, representing the medial-to-lateral relationship in effective soft-tissue constraints, and the flexion-state metric is defined as $Q = K_{post} / K_{med}$, representing posterior drive relative to medial anchoring. **f**, KPE-derived S–Q state map showing the relationship between soft-tissue constraint state and differential rollback pattern R. The model separates three kinematic regimes: paradoxical anterior translation ($R < 0$), lateral-pivot motion ($0 < R < 1$), and medial-pivot motion ($R > 1$). Increasing S narrows the admissible range of Q, whereas variation

in Q within the admissible region allows transitions among rollback regimes. The hatched area denotes combinations for which no admissible solution is obtained under the model, and the critical S marks the upper extension-state boundary beyond which the admissible kinematic solution space becomes restricted.

Defining the quantitative solvability boundary for soft-tissue intervention

To mathematically extract the constraint parameter S from the intraoperative Solver data, we modeled the knee joint in extension as a simplified beam–spring system, representing the medial and lateral collateral ligaments as equivalent springs with stiffnesses K_{med} and K_{lat} respectively (Fig. 3e). Accordingly, S serves as the direct quantitative index of the patient's native medial-lateral soft-tissue constraint asymmetry.

To clinically validate the guiding role of S in surgical decision-making, we analyzed intraoperative data from 356 knees undergoing primary robot-assisted cruciate-retaining TKA. The baseline S value was recorded strictly after the initial bone cuts but prior to any soft-tissue release. Clinically, soft-tissue release was triggered if and only if adjusting the bone cuts within the permissible boundary failed to achieve the preset gap balance.

The data revealed that the baseline S was significantly higher in knees requiring release compared to the non-release group (1.43 ± 0.30 vs. 1.20 ± 0.25; Welch's t-test, $P < 0.001$; Fig. 4a). Following targeted soft-tissue release, the S value in the intervention group decreased to 1.00 ± 0.19, effectively restoring the native constraint symmetry (Fig. 4a).

Supervised receiver operating characteristic (ROC) curve analysis predicted a cutoff value of $S = 1.28$ for determining the necessity of soft-tissue release (Fig. 4b). Complementary unsupervised Bayesian Gaussian mixture model (GMM) analysis identified two distinct constraint states (low

S and high *S*), yielding a distribution boundary at $S = 1.33$ (95% CI, 1.25–1.40; Fig. 4c). Given the strong concordance between these two independent analyses, we established $S \approx 1.3$ as the intraoperative measurable equivalent of the upper bound of the KCE-defined solvable domain. Applying this empirical threshold to our cohort, 265 knees (74.4%) fell within the boundary ($S < 1.3$), whereas 91 knees (25.6%) exceeded it ($S \geq 1.3$) (Fig. 4d).

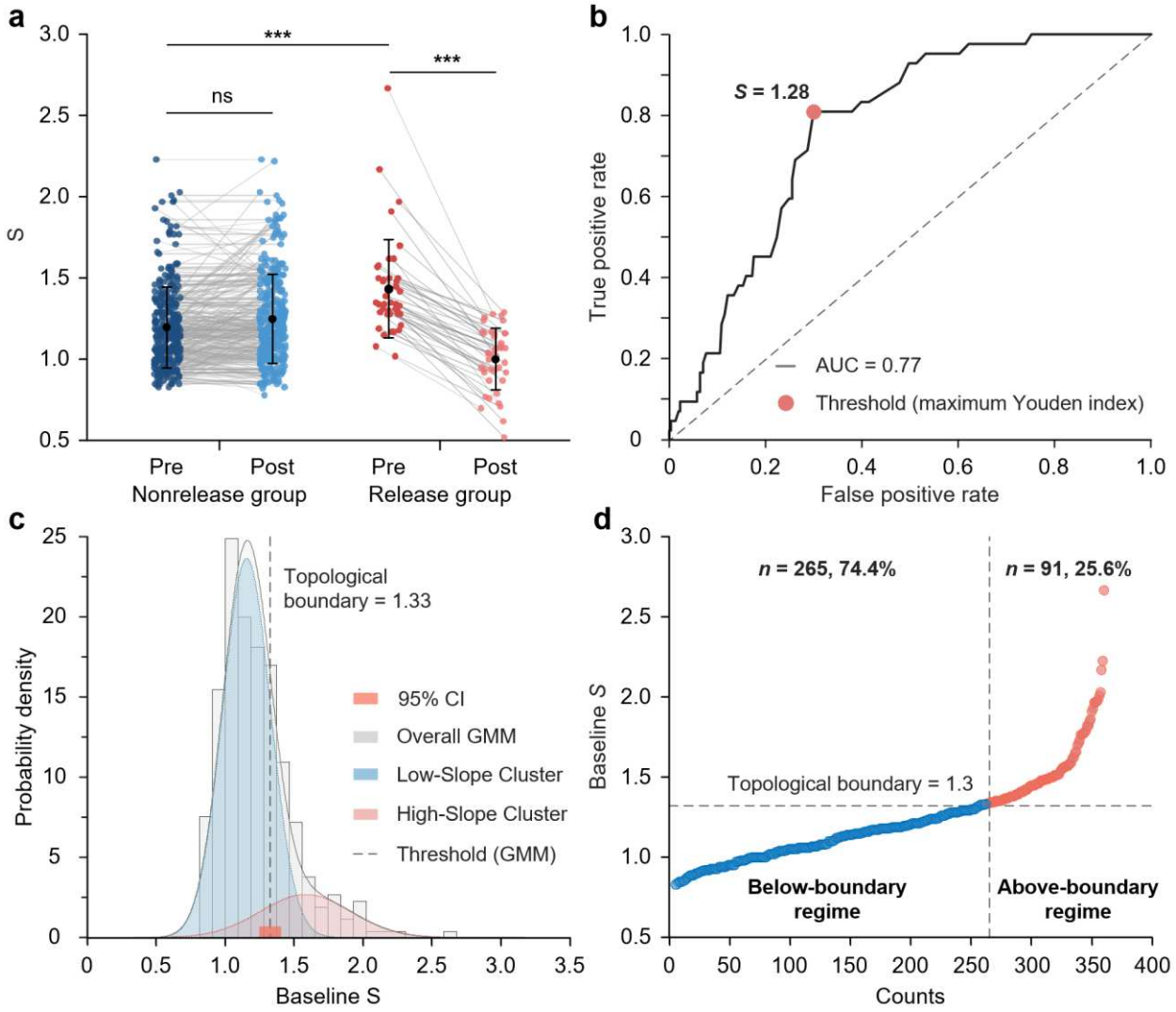


Fig 4. | Retrospective analyses of *S* identified an extension-state solvability boundary. a, Paired baseline and final intraoperative *S* values in the non-release ($n = 314$) and release ($n = 42$) groups. Baseline *S* was measured after initial alignment and trial component positioning and

before any soft-tissue release. Error bars indicate the mean ± s.d. Within-group changes from baseline to final S were assessed using two-sided paired Student's t-tests. Baseline *S* values were compared between the release and non-release groups using a two-sided Welch's t-test ***$P <$ 0.001; ns, not significant. **b**, Supervised ROC analysis of baseline *S* for distinguishing release-required from non-release knee. **c**, Unsupervised Bayesian GMM of the baseline *S* distribution. The posterior class-density curves identified lower-S and higher-S latent constraint phenotypes. Their intersection defined a distributional boundary at $S \approx 1.33$ (95% CI, 1.25–1.40). **d**, The supervised ROC and unsupervised GMM analyses independently interrogated the same underlying extension-state boundary and produced closely aligned estimates; their convergence was therefore summarized as $S \approx 1.3$. AUC, area under the curve; CI, confidence interval; GMM, Gaussian mixture model; ROC, receiver operating characteristic; s.d., standard deviation.

The flexion-state metric *Q* predicts tibiofemoral rollback transitions

We next evaluated whether the flexion metric *Q*, together with *S*, could stratify the femoral condyle rollback pattern predicted by the KPE. We analyzed 362 intraoperative kinematic trajectories from 131 knees, extracting paired *Q* and *R* values.

We performed threshold scan analyses at the KPE-defined inflection points ($R = 0$ and $R = 1$), alongside a stringent endpoint of $R = 1.5$ representing a strict medial-pivot phenotype. The scan curves converged to an initial inflection signal near $Q \approx 0.35$, whereas the $R = 1.5$ phenotype exhibited a secondary local peak near $Q \approx 0.45$ (Fig. 5a,b). Following the exclusion of trajectories with $R < 0$, repeated fivefold cross-validation localized the critical $R = 1$ transition strictly near $Q \approx 0.40$ (Fig. 5c). Consequently, we defined a functional transition zone spanning (0.35–0.45). Within this interval, the lower bound $Q \approx 0.35$ marks the entry into the posterior

rollback phase, whereas $Q \approx 0.40$ acts as the fundamental switch shifting the kinematics from an outer to an inner pivot (Fig. 5d). Posterior tibial slope was further examined as a local modifier of the strict medial-pivot phenotype (Fig. 5e).

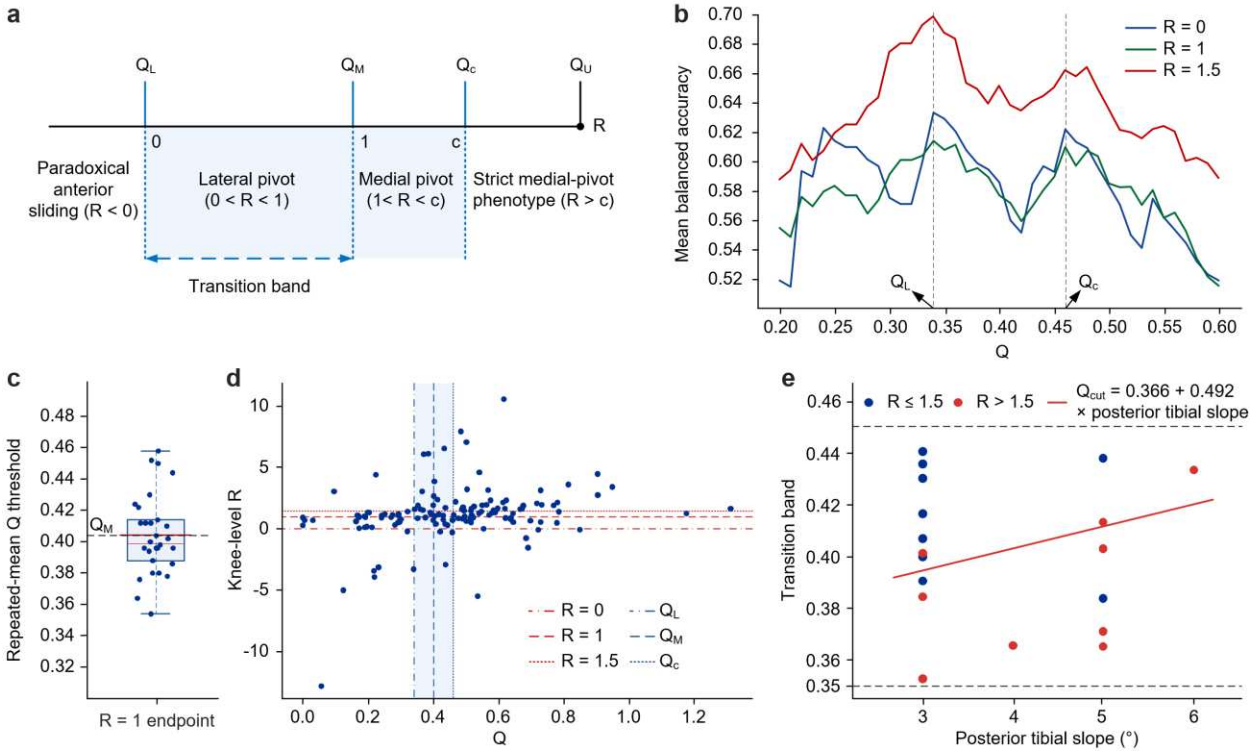


Fig 5. | Rollback transitions cluster within a *Q*-defined transition band, with local slope-associated enrichment of the strict medial-pivot phenotype.

a, Schematic of the KPE-defined rollback-phase structure along Q. The corresponding empirical transition signals are examined in **b–d**. Q_L, Q_M and Q_U denote the R =0 boundary, the $R = 1$ lateral-to-medial pivot transition and the upper admissible boundary, respectively; Q_c marks the prespecified strict medial-pivot reference at $R = c$ ($c = 1.5$). **b**, Fivefold cross-validated threshold scanning for the KPE-defined transitions at $R = 0$, $R = 1$ and the prespecified strict medial-pivot endpoint at $R = 1.5$, using 362 path-level recordings from 131 knees. The dashed lines indicate the principal lower transition signal near $Q \approx 0.35$ and the secondary $R > 1.5$-associated support

peak near $Q \approx 0.45$. **c**, Repeated fivefold cross-validation of the $R = 1$ transition after exclusion of paths with $R < 0$. The analysis included 316 valid paths from 124 knees, comprising 113 paths with $0 < R < 1$ and 203 paths with $R > 1$. **d**, Distribution of energy-weighted R against Q in 131 knees. The vertical dashed lines indicate the lower edge at $Q \approx 0.35$, transition center at $Q \approx 0.40$ and upper edge at $Q \approx 0.45$ of the transition band. The horizontal reference lines indicate the KPE-defined transitions at $R = 0$, $R = 1$ and the prespecified strict medial-pivot endpoint at $R = 1.5$. The shaded region highlights the $Q \approx 0.35$–0.45 transition band. **e**, Local association of posterior tibial slope with the strict medial-pivot phenotype within the $Q \approx 0.35$–0.45 transition band. The intercept and slope coefficient were estimated from a classification model using Q and posterior tibial slope to distinguish knees with $R > 1.5$ from those with $R < 1.5$.

Retrospective validation links the flexion-state metric to postoperative functional recovery

To validate the predictive capacity of the KPE regarding femoral condyle rollback patterns, repeated path-level trajectories were integrated via energy weighting to derive a representative R value per knee. The persistence of mixed patterns within $Q \approx 0.35$ confirmed this interval as a continuous transition band rather than a discrete boundary. While secondary covariance analysis indicated that the posterior tibial slope could locally modulate the boundary for the $R > 1.5$ phenotype (Fig. 5e), cross-validation confirmed that Q remains the primary driver of the rollback structure (Extended Data Fig. 1).

Building upon this transition band, we next investigated whether intraoperative Q correlated with postoperative functional recovery in a retrospective cohort of 84 knees with complete follow-up data. Exploratory analyses across standard clinical scores—including ROM, KOOS, WOMAC,

and FJS-12 (Table 1)—identified an outcome-associated window of $0.28 \leq Q \leq 0.40$ (comprising 12 knees, with 72 knees outside). This outcome-derived window partially overlapped with, but was analytically distinct from, the KPE-associated rollback transition band of $Q \approx 0.35–0.45$.

Patients within the $0.28 \leq Q \leq 0.40$ window demonstrated superior functional outcomes compared to those outside. Specifically, they achieved a greater range of motion (125.0° [IQR, 103.8–138.8] vs. 110.0° [IQR, 95.0–120.0]; $P = 0.013$) and more favorable KOOS subscores for Symptoms (96.4 vs. 89.3; $P = 0.047$), Activities of Daily Living (96.3 vs. 91.9; $P = 0.020$), and Quality of Life (90.6 vs. 81.3; $P = 0.034$). Furthermore, they exhibited lower WOMAC scores (3.5 vs. 7.0; $P = 0.016$) and higher Forgotten Joint Scores (90.6 vs. 65.6; $P = 0.028$) (Table 1).

Robustness tests, including bootstrap, permutation, and boundary-sensitivity analyses, confirmed the stability of this directional consistency across all clinical endpoints (Extended Data Fig. 2a-d). While these retrospective findings identify $0.28 \leq Q \leq 0.40$ as a promising outcome-associated intraoperative window, prospective interventional studies are warranted to determine whether actively guiding Q into this specific interval directly enhances postoperative functional recovery.

Table 1. Postoperative outcomes in knees with intraoperative *Q* values within versus outside the 0.28–0.40 window.

Clinical outcomes	$0.28 \leq Q \leq 0.40$ ($n = 12$)	$Q < 0.28$ or $Q > 0.40$ ($n = 72$)	Effect size (Rank-biserial r)	Standard P value (MWU)	Exact permutation P value (10,000 resamples)	Bootstrapped 95% CI
ROM (°)	125.0 [103.8, 138.8]	110.0 [95.0, 120.0]	0.40	0.013*	0.013*	[0.55, 23.72]
Pain	95.8 [89.6, 100.0]	91.7 [83.3, 100.0]	0.24	0.085	0.084	[-0.61, 8.62]
Symptoms	96.4 [87.5, 100.0]	89.3 [82.1, 96.4]	0.30	0.047*	0.041*	[0.68, 10.39]
ADL	96.3 [94.1, 98.5]	91.9 [88.2, 95.6]	0.37	0.020*	0.019*	[0.80, 8.06]
Sport/Recreation	37.5 [30.0, 60.0]	30.0 [20.0, 30.0]	0.16	0.187	0.257	[-8.29, 17.22]
QoL	90.6 [81.3, 100.0]	81.3 [68.8, 100.0]	0.33	0.034*	0.033*	[3.08, 18.94]
WOMAC score	3.5 [1.5, 5.5]	7.0 [3.0, 13.5]	-0.39	0.016*	0.015*	[-7.61, -1.70]
FJS-12 (points)	90.6 [65.6, 100.0]	65.6 [38.5, 90.6]	0.35	0.028*	0.027*	[-1.10, 32.08]

Data are medians [IQRs]. Q, flexion-state metric; ADL, Activities of Daily Living; BCa, bias-corrected and accelerated; CI, confidence interval; FJS-12, 12-item Forgotten Joint Score; IQR, interquartile range; KOOS, Knee injury and Osteoarthritis Outcome Score; MWU, Mann–Whitney U test; QoL, Quality of Life; ROM, range of motion; WOMAC, Western Ontario and McMaster Universities Osteoarthritis Index. Higher KOOS and FJS-12 scores and lower WOMAC scores indicate better outcomes. Effect sizes are rank-biserial correlations (r); positive values favor the in-window group for outcomes in which higher scores are better, whereas negative values favor the in-window group for WOMAC. P values are two-sided.

Discussion

The formulation of the KCE fundamentally deepens our understanding of TKA by quantitatively delineating the interplay among the core elements of the surgery: soft-tissue constraints, component positioning, and implant geometry. The KCE defines component positioning and implant geometry as tunable variables, while treating soft-tissue constraints as a constant. This reveals that the historical convention of routinely performing soft-tissue releases to resolve

kinematic conflict is conceptually flawed, as it indiscriminately alters the native constraint state rather than optimizing the surgical variables to satisfy it. Soft-tissue release is justified if and only if adjusting the bone cuts within the permissible boundary fails to resolve the kinematic conflict. The Solver acts as the critical diagnostic tool to evaluate this condition, objectively determining whether the soft tissues actually require releasing. While evolving alignment philosophies[18-20] represent beneficial attempts to mitigate kinematic conflict through alternative bone cuts, such optimizations often serve as mere categorical approximations rather than mathematically personalized solutions. By coupling bone resection to soft-tissue constraints, the KCE proves that personalized component positioning is mechanically imperative. Similarly, by embedding implant geometry as an independent variable, the equation illuminates personalized implant design as a pivotal frontier in TKA. Distilled from the KCE through dimensional reduction, the Kinematic Pattern Equation (KPE) acts as a vital bridge connecting surgical planning, joint kinematics and clinical outcomes, providing an actionable tool for intraoperative optimization. This framework drives a profound paradigm shift, transitioning TKA from an experience-based empirical practice to a rigorous analytical one.

The clinical translation of this analytical framework hinges on the development of the Solver, which represents a disruptive breakthrough in overcoming the historical limitations of soft-tissue assessment. While conventional tools rely on subjective tactile feedback or static, discrete tension measurements[21-23], the Solver dynamically maps the continuous elastic behavior of the soft-tissue envelope at key flexion angles. Functioning as the computational engine, it parameterizes the structural stiffness (k) for the KCE and drives the extraction of the constraint indices (S and Q) for the KPE, thereby operationalizing the theoretical equations. Most notably, the high-fidelity data generated by the solver reveal the profound, inherent diversity of native

human soft-tissue constraints. The wide spectrum of baseline S values observed across our cohort definitively exposes the inadequacy of binary clinical classifications (e.g., “tight” versus “loose”) and challenges the traditional pursuit of universal gap symmetry. By decoding each patient’s unique soft-tissue constraint signature, the solver empowers surgeons to move beyond rigid, uniform surgical protocols toward truly personalized biomechanical optimization in TKA.

Guided by the principles of the KCE and KPE, our findings elucidate the direct clinical utility of these parameters. Specifically, the extension-state metric S (with a critical threshold near 1.3) serves as an actionable surgical threshold, dictating precisely when bone-cut adjustments become insufficient and soft-tissue release becomes necessary. In the flexion phase, the parameter Q reflects the posterior tethering force, which mechanically dictates the tibiofemoral rollback pattern. While the continuous kinematic transition band (Q = 0.35–0.45) illustrates a fluid biomechanical shift, our exploratory analysis successfully pinpointed a specific outcome-associated window ($0.28 \leq Q \leq 0.40$). The ability to establish this clear linkage—from intraoperative solver data to kinematic patterns, and ultimately to functional recovery—validates the core premise of our analytical paradigm. It demonstrates that guiding intraoperative metrics toward this quantified therapeutic window can directly translate to superior clinical outcomes.

Several limitations warrant consideration. First, the underlying mechanical model relies on simplified equivalent spring representations, and posterior constraints were evaluated exclusively at a fixed 90° flexion. Second, although bolstered by rigorous cross-validation and sensitivity analyses, the outcome-associated window was identified through exploratory screening within a retrospective cohort[24]. The localized subset (n = 12) within this optimal range necessitates further validation through larger, independent prospective trials. Finally, as our analysis was restricted to

posterior-cruciate-ligament-retaining (CR) prostheses, the generalizability of these findings to other implant designs remains to be established[25-27]. Despite these limitations, this rigorous analytical procedure fundamentally harmonizes stability and mobility in TKA. Future prospective interventional studies will determine whether actively steering intraoperative parameters into these defined functional windows can reliably enhance long-term postoperative recovery.

Methods

Study design and analytical workflow

This study combined theoretical model development with retrospective analyses of intraoperative biomechanical data and postoperative clinical outcomes in knees that underwent robot-assisted total knee arthroplasty (TKA). The analytical workflow comprised three components: derivation of the mechanical framework, quantification of intraoperative soft-tissue and kinematic variables, and evaluation of their associations with postoperative outcomes. This study was approved by the Institutional Review Board of Beijing Jishuitan Hospital (approval No. K-2023-008–00). Written informed consent for participation and use of clinical data was obtained from all participants.

Clinical cohort

Consecutive primary robotic-assisted TKA performed at Beijing Jishuitan Hospital between 2021 and 2025 were screened. Sample sizes were determined by the availability of the data required for each analytical module in the institutional robotic TKA registry rather than by an a priori powered clinical trial. Eligible knees underwent primary robotic-assisted TKA using a posterior cruciate-retaining prosthesis and had the intraoperative solver recordings required for the corresponding analysis. Revision procedures, knees with incomplete sensor or operative documentation, discontinuous or invalid kinematic recordings for trajectory-based analyses, and knees missing variables required for the relevant analytical module were excluded.

Data completeness defined three strictly nested cohorts. The full solver cohort comprised 356 knees with complete intraoperative solver data for calculation of S and Q. Within this cohort, 131 knees provided 362 valid intraoperative kinematic paths for analyses relating solver-derived Q to

trajectory-derived *R*. Within these 131 knees, 84 knees had a minimum clinical follow-up of six months and formed the postoperative outcome cohort used to evaluate the association between the outcome-associated *Q* window and postoperative outcomes. Outcomes included range of motion, the KOOS[28], WOMAC[29], and FJS-12[30]. All cohort sizes are reported as knees because some patients contributed bilateral procedures.

Robotic-assisted TKA and surgical workflow

All TKA procedures were performed by senior arthroplasty surgeons, each with more than 10 years of arthroplasty experience, using a standardized robotic-assisted workflow that allowed surgeon-specific adaptation. All procedures were performed using the TiRobot system (TINAVI Medical Technologies, Beijing, China). The system was used for surgical planning, robotic-guided bone resection and optical tracking during intraoperative passive flexion–extension.

A TKA Balance Solver (Tinavi Medical Technologies, Beijing, China) was used after bone preparation and trial reduction to acquire compartment-level force–gap data. The device independently recorded medial and lateral gap responses under controlled joint-distraction loading, allowing angle-specific gap matrices to be generated for subsequent stiffness decoupling and calculation of the solver-derived metrics. The optical tracking system recorded relative tibiofemoral motion during passive flexion–extension, from which medial and lateral contact-point trajectories were reconstructed using the registered joint geometry.

To reduce procedural variability, all knees underwent a standardized sequential bone-resection protocol. Before soft-tissue release, compartmental gaps were assessed under controlled loading using the intraoperative solver. The diagonal line on the solver plot represented equal medial and lateral gaps. Based on iterative institutional experience accumulated during the development and

clinical implementation of the solver, the positional target, defined before the study, required the lateral gap to exceed the medial gap by 0–1 mm in extension and 0–2 mm in flexion, with the mediolateral offset remaining within 0–2 mm throughout the measured flexion–extension range[31]. These criteria were used to determine whether residual imbalance could be corrected through component selection and component positioning alone or whether soft-tissue release was required to achieve balance. Soft-tissue release was performed only when these predefined gap-balance targets could not be achieved through component selection and component positioning[31].

Device Characteristics and the "TKA Solver" Concept

The soft-tissue balancing device consists of two independent spreading actuators and a connected vertical lifting drive motor (Fig. 2a). Fabricated from medical-grade stainless steel, the device withstands standard intraoperative sterilization protocols. Unlike conventional static spacer blocks, this device dynamically opens the tibiofemoral space, applying a progressive distraction force via the motor and recording the continuous force-displacement response. The applied tension ranges from 30 N to 100 N (in 5 N increments), aligning with established physiological tension levels of periarticular soft tissues.

Following the initial tibial resection, the Solver is introduced to progressively distract the joint space. It captures the medial and lateral tibiofemoral gaps across the predefined tension gradient (Fig. 2e). Continuous gap-tension mappings are recorded at full extension (0°), early flexion (10°), and deep flexion (90°) to evaluate the multi-angle soft-tissue envelope status dynamically.

Mathematical formulation of the KCE and KPE

The Kinematic Conflict Equation (KCE) was formulated to represent the reconstructed knee as a coupled alignment–geometry–constraint system. Generalized alignment (a) and implant

geometry (g) define the surgical configuration space, whereas the patient-specific soft-tissue constraint state (k) modulates the system response. Kinematic conflict (u) was defined as the mismatch between the imposed reconstruction and the state permitted by the soft-tissue constraints. The KCE was derived from a variational formulation in which equilibrium corresponds to a stationary state of the system-level conflict functional.

The kinematic pattern equation (KPE) was derived as a reduced representation of this system at the tibiofemoral contact interface. A quasi-static force balance was established between geometry-dependent resistance and the posterior driving component, yielding a relationship between the differential rollback ratio R, the measurable soft-tissue metrics S and Q, and geometry-dependent coefficients determined by implant geometry, local contact state and posterior tibial slope. The KPE therefore provides the low-dimensional relationship between soft-tissue constraint state and rollback phenotype used in the subsequent boundary analyses. Full derivations of the KCE and KPE, their solvability conditions and the mathematical relationship between the two formulations are provided in Supplementary Methods A1–A3.

Intraoperative calculation of *S*, *Q* and *R*

Intraoperative solver data from the full cohort of 356 knees were used to calculate the extension-state metric S and flexion-state metric Q (Fig. 3e and Supplementary Methods A4). Medial and lateral force–gap responses were converted to compartment-level effective stiffnesses using the prespecified beam–spring decoupling framework. For the extension-state analysis, the solver matrix was fitted using robust linear regression in MATLAB R2021a with bisquare weighting and default tuning parameters, from which S was obtained. For the flexion-state analysis, the same decoupling framework was applied to early-flexion and 90° measurements. For estimation

of the flexion-state coordinate Q, early-flexion collateral contributions at 90° were scaled using nominal medial and lateral relaxation coefficients.

Concurrently, tibiofemoral contact-point trajectories were reconstructed from robotic tracking data acquired during passive flexion–extension. For each valid trajectory, medial and lateral anteroposterior displacements were calculated over the 30°–90° flexion interval and used to obtain a path-level differential rollback ratio R (Supplementary Methods A5). Path-level R values were used for rollback-phase threshold analyses. For knees with multiple valid trajectories, repeated paths were integrated using the prespecified energy-weighting procedure to obtain a representative knee-level trajectory and corresponding knee-level R (Extended Data Fig. 3), which were used for knee-level Q–R analyses. Full derivations of S and Q, together with the beam–spring decoupling assumptions, are provided in Supplementary Methods A4; detailed trajectory processing, energy-weighted integration and knee-level construction of R are provided in Supplementary Methods A5.

Identification of the *S* solvability boundary

Baseline S values were used to estimate the mathematical upper boundary of the extension-state solvable region. Two complementary approaches were applied. First, release status was used as the protocol-defined intraoperative label in a supervised ROC analysis. Knees in which soft-tissue release was performed because the prespecified positional gap targets could not be achieved after initial alignment and component-position optimization were designated as the positive class, whereas knees achieving these targets without release were designated as the negative class. Sensitivity was defined as the proportion of release-required knees correctly classified, and specificity as the proportion of nonrelease knees correctly classified. The ROC-

derived cutoff was selected by maximizing the Youden index, J = sensitivity+specificity−1[32]. Larger J values indicate better combined sensitivity and specificity. Classification performance was summarized using the area under the ROC curve (AUC), for which 0.5 indicates chance-level discrimination and 1.0 indicates perfect discrimination.

Second, Bayesian Gaussian mixture modeling was applied to the distribution of baseline S values without using release status as an input label. Posterior class probabilities were used to identify two naturally separable constraint phenotypes. The intersection of the posterior class-density curves was defined as the unsupervised GMM-derived boundary.

The final S threshold was determined by comparing the supervised ROC-derived cutoff with the unsupervised GMM-derived boundary. Agreement between the two estimates was used to define the extension-state S solvability boundary for subsequent cohort stratification.

Identification of *Q*-defined rollback phase boundaries

Path-level R values were used to define rollback phases, and corresponding Q boundaries were estimated by sequential threshold scanning across the observed Q range. The two primary KPE-defined transitions were $R = 0$, separating paradoxical anterior translation from posterior rollback, and $R = 1$, separating lateral-pivot from medial-pivot rollback. For the $R = 1$ analysis, paths with $R < 0$ were excluded. Threshold performance was evaluated using repeated fivefold cross-validation, with mean balanced accuracy (MBA) calculated across validation folds and repeats; the threshold yielding the highest MBA was taken as the estimated boundary.

Posterior tibial slope was evaluated as a local modifier within the low-Q transition region using the stricter medial-pivot endpoint $R > 1.5$. Classification models based on Q alone and on Q plus posterior tibial slope were compared using balanced accuracy, sensitivity, specificity and AUC,

and the fitted decision boundary was used to characterize slope-dependent displacement of the local Q boundary.

Boundary robustness was further assessed in three nested knee-level subsets: all evaluable knees, a stable-basin subset in which all available path-level R values remained within a single rollback phase region, and a high-confidence stable subset additionally restricted to a within-knee phase-angle range $\Delta\Phi \le 0.15$ radians, where $\Phi = \arctan(R)$. Boundary performance was reassessed in each subset to evaluate sensitivity to within-knee trajectory variability.

Clinical outcome analysis of the outcome-derived *Q* window

The postoperative outcome cohort was used to examine the association between intraoperative Q and postoperative function at the final follow-up (> 6 months). Outcomes included range of motion (ROM), Knee injury and Osteoarthritis Outcome Score (KOOS) subscales, Western Ontario and McMaster Universities Osteoarthritis Index (WOMAC), and Forgotten Joint Score-12 (FJS-12).

Candidate lower and upper Q boundaries were systematically scanned, with knees classified as in-window when their Q values fell within both boundaries and as out-of-window otherwise. The interval ($0.28 \le Q \le 0.40$) was identified as the exploratory outcome-derived window because it showed the most directionally consistent associations across the prespecified functional and patient-reported outcomes rather than being selected on the basis of any single endpoint. The robustness of this interval was examined across adjacent candidate window definitions. Group comparisons and statistical procedures are described in the Statistical analysis section.

Statistical analysis

Continuous variables were assessed for normality using the Shapiro–Wilk test[33]. Normally distributed variables were summarized as mean ± s.d., and nonnormally distributed variables as median (interquartile range). Categorical variables were summarized as counts and percentages. All statistical tests were two-sided, and $P < 0.05$ was considered statistically significant.

For the Q-based classification of R-defined rollback phases, candidate Q thresholds were scanned across the observed Q range. Classification performance was evaluated using repeated fivefold cross-validation. For each validation fold, balanced accuracy (BA) was calculated as BA = (sensitivity + specificity) / 2, where sensitivity and specificity were calculated with the higher-R phase designated as the positive class. The threshold with the highest MBA was taken as the estimated boundary. Sensitivity, specificity and AUC were additionally reported. For the $R = 1$ transition, paths with $R < 0$ were excluded before threshold estimation. A stricter medial-pivot phenotype was defined as $R > 1.5$, and models based on Q alone and on Q plus posterior tibial slope were compared using BA, sensitivity, specificity and AUC to assess local modification of the Q boundary by posterior tibial slope.

For each candidate interval, knees were classified as inside or outside the interval, and the direction of between-group differences was evaluated across the prespecified postoperative outcomes. The resulting $Q = 0.28–0.40$ interval was treated as exploratory and outcome-derived. Between-group comparisons for the final window were performed using the Mann–Whitney U-test for nonnormally distributed outcomes, with rank-biserial correlation used as the effect-size measure. Exact permutation tests with 10,000 resamples were used as robustness checks. Bias-corrected and accelerated bootstrap analysis with 10,000 iterations was used to estimate 95%

confidence intervals for between-group differences[34]. Sensitivity analyses repeated the comparisons across adjacent candidate *Q*-window definitions.

Data Availability

The datasets generated during and/or analyzed during the current study are available from the corresponding author on reasonable request.

References

1. Kurtz, S., Ong, K., Lau, E., Mowat, F. & Halpern, M. Projections of primary and revision hip and knee arthroplasty in the United States from 2005 to 2030. J. Bone Joint Surg. Am. 89, 780–785 (2007).
2. DeFrance, M. J. & Scuderi, G. R. Are 20% of Patients Actually Dissatisfied Following Total Knee Arthroplasty? A Systematic Review of the Literature. J. Arthroplasty 38, 594–599 (2023).
3. Gusho, C., Hoskins, W. & Ghanem, E. No Superiority of Total Knee Arthroplasty Alignment Philosophies: A Network Meta-Analysis Comparing Mechanical, Anatomical, Kinematic, Restricted Kinematic, and Functional Alignment Among Randomized Controlled Trials. JBJS Rev. 13, e25.00101 (2025).
4. De, C., Tahir, M., Pierce, T., Awasthi, P. & Fonseca, P. C. Why Are Patients Without Identifiable Etiology of Failure Dissatisfied Following Total Knee Arthroplasty: A Systematic Review and Meta-Analysis. J. Knee Surg. 38, 717–724 (2025).
5. Barroso Rosa, S. et al. Influence of Total Knee Arthroplasty Alignment on Soft-Tissue Balance and Pivot Patterns: A Randomized Controlled Trial of Kinematic Versus Mechanical Alignment. J. Arthroplasty 40, 3155–3161 (2025).
6. Naito, Y., Tone, S., Kobayashi, G. & Hasegawa, M. Comparison of Clinical Outcomes and Soft Tissue Laxity Between Robot-Assisted Functionally and Mechanically Aligned Total Knee Arthroplasty. Cureus 17, e91084 (2025).
7. Vermue, H. et al. An Asymmetric Medio-Lateral Flexion Laxity Target Yields Excellent Results in Robotic-Assisted Total Knee Arthroplasty With Functional Knee Positioning. J. Arthroplasty 41, 2411–2417.e1 (2026).
8. Young, S. W. et al. The John N. Insall Award: Functional Versus Mechanical Alignment in Total Knee Arthroplasty: A Randomized Controlled Trial. J. Arthroplasty 40, S20–S30.e2 (2025).
9. MacDessi, S. J., Wood, J. A., Diwan, A. & Harris, I. A. Intraoperative pressure sensors improve soft-tissue balance but not clinical outcomes in total knee arthroplasty: a multicentre randomized controlled trial. Bone Joint J. 104-B, 604–612 (2022).
10. Tran, J. Y. S. et al. A comparison on the clinical outcomes of using intraoperative load sensors versus manual balancing in total knee arthroplasty: a systematic review and meta-analysis. J. Orthop. Surg. Res. 20, 970 (2025).
11. Orsi, A. D. et al. Soft Tissue Balance Profiles Differ Between Manual and Robotically Assessed Gaps in Total Knee Arthroplasty. Int. J. Med. Robot. 21, e70124 (2025).
12. Fu, X. et al. Comparison of robotic-assisted total knee arthroplasty: an updated systematic review and meta-analysis. J. Robot. Surg. 18, 292 (2024).
13. Sodhi, K. et al. Robotic-assisted total knee arthroplasty with MAKO is associated with improved functional outcomes: a systematic review and meta-analysis. Bone Jt Open 6, 1382–1393 (2025).

14. Scholl, L. Y. et al. Robotic-assisted Total Knee Arthroplasty Technology Provides a Repeatable and Reproducible Method of Assessing Soft Tissue Balance. J. Knee Surg. 37, 607–611 (2024).
15. Sharma, A. K. et al. Ligament Tension and Balance before and after Robotic-Assisted Total Knee Arthroplasty - Dynamic Changes with Increasing Applied Force. J. Knee Surg. 37, 128–134 (2024).
16. Lee, J. H., Kwon, S. C., Hwang, J. H., Lee, J. K. & Kim, J. I. Functional alignment maximises advantages of robotic arm-assisted total knee arthroplasty with better patient-reported outcomes compared to mechanical alignment. Knee Surg. Sports Traumatol. Arthrosc. 32, 896–906 (2024).
17. Yang, D. et al. Soft tissue elasticity in total knee arthroplasty: An in vivo quantitative analysis. Clin. Biomech. 120, 106335 (2024).
18. MacDessi, S. J. et al. The language of knee alignment: updated definitions and considerations for reporting outcomes in total knee arthroplasty. Bone Joint J. 105-B, 102–108 (2023).
19. Davey, M. S., Hughes, A. J., Sculco, P. K. & Star, A. M. Alignment Philosophies in Total Knee Arthroplasty: A Comprehensive Narrative Review. Arthroplast. Today 37, 101940 (2026).
20. Ettinger, M., Tuecking, L. R., Savov, P. & Windhagen, H. Higher satisfaction and function scores in restricted kinematic alignment versus mechanical alignment with medial pivot design total knee arthroplasty: A prospective randomised controlled trial. Knee Surg. Sports Traumatol. Arthrosc. 32, 1275–1286 (2024).
21. Weiner, T. R., Shah, R. P., Neuwirth, A. L., Geller, J. A. & Cooper, H. J. Soft tissue laxity is highly variable in patients undergoing total knee arthroplasty. Arthroplasty 6, 45 (2024).
22. Inui, H. et al. Assessment of joint laxity following total knee arthroplasty: A comparison of tensioner device, navigation, and robot evaluation. Knee 56, 397–406 (2025).
23. Becker, R. et al. Mean distraction force applied in tension-controlled ligament-balanced total knee arthroplasty: A systematic review and meta-analysis. Knee Surg. Sports Traumatol. Arthrosc. 33, 2498–2526 (2025).
24. Varma, S. & Simon, R. Bias in error estimation when using cross-validation for model selection. BMC Bioinformatics 7, 91 (2006).
25. Zhu, K. et al. Effect of Posterior Cruciate Ligament Resection on Gap Balancing in Robot-assisted Total Knee Arthroplasty. Orthop. Surg. 16, 1929–1938 (2024).
26. Alloun, N. et al. Posterior cruciate ligament resection increases intraoperative lateral and medial flexion laxity during total knee arthroplasty. Int. Orthop. 49, 613–619 (2025).
27. Vermue, H., Batailler, C., Budhiparama, N. & Lustig, S. Posterior Cruciate Ligament Retention Does Not Influence Clinical Outcomes in Medial Pivot Total Knee Arthroplasty: A Systematic Review and Meta-Analysis. J. Arthroplasty 40, 3342–3348 (2025).
28. Roos, E. M. & Lohmander, L. S. The Knee injury and Osteoarthritis Outcome Score (KOOS): from joint injury to osteoarthritis. Health Qual. Life Outcomes 1, 64 (2003).
29. Bellamy, N., Buchanan, W. W., Goldsmith, C. H., Campbell, J. & Stitt, L. W. Validation study of WOMAC: a health status instrument for measuring clinically important patient relevant outcomes to antirheumatic drug therapy in patients with osteoarthritis of the hip or knee. J. Rheumatol. 15, 1833–1840 (1988).

30. Behrend, H., Giesinger, K., Giesinger, J. M. & Kuster, M. S. The "forgotten joint" as the ultimate goal in joint arthroplasty: validation of a new patient-reported outcome measure. J. Arthroplasty 27, 430–436.e1 (2012).
31. Chen, M. et al. Using sequential bone cutting to titrate soft tissue balance in total knee arthroplasty effectively minimizes soft tissue release. BMC Musculoskelet. Disord. 24, 866 (2023).
32. Youden, W. J. Index for rating diagnostic tests. Cancer 3, 32–35 (1950).
33. Shapiro, S. S. & Wilk, M. B. An analysis of variance test for normality (complete samples). Biometrika 52, 591–611 (1965).
34. Efron, B. Better bootstrap confidence intervals. J. Am. Stat. Assoc. 82, 171–185 (1987).

Acknowledgements

We would like to thank Y. Wang from the Department of Medical Statistics, Fuwai Hospital for technical support in statistical methodology.

Ethics declarations

Competing interests

Yixin Zhou is the inventor of the “Solver” device discussed in this manuscript. All other authors declare no competing interests.

Supplementary Information

Supplementary information includes:

- Equation S1 to S43 for supplementary equations

Funding

This work was supported by:

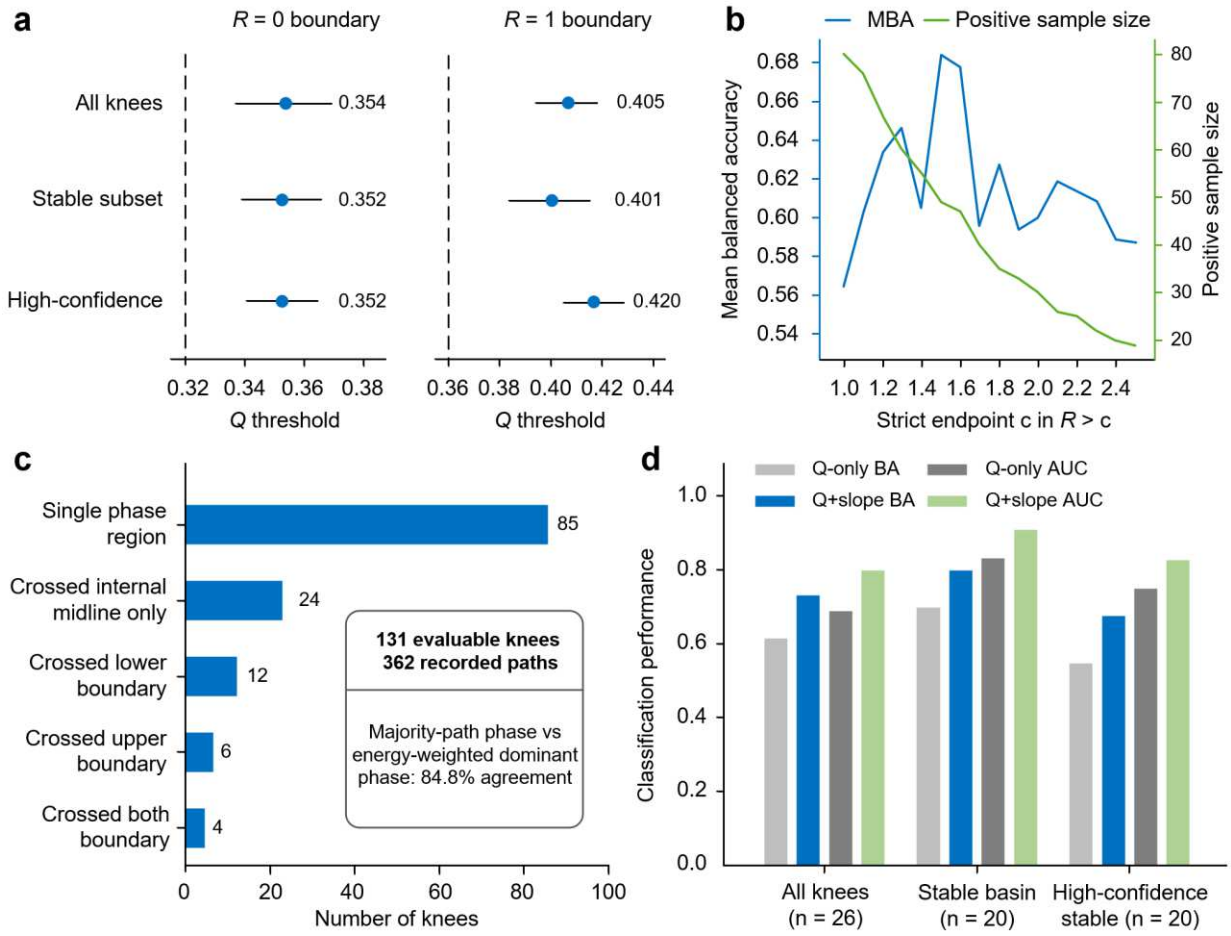
Beijing Natural Science Foundation (YXZ, L254008)

Beijing Municipal Health Commission (YXZ, DL, No. BJRITO-RDP)

Beijing Natural Science Foundation (DL, No. L2602101)

National Natural Science Foundation of China (DL, No. T2600291)

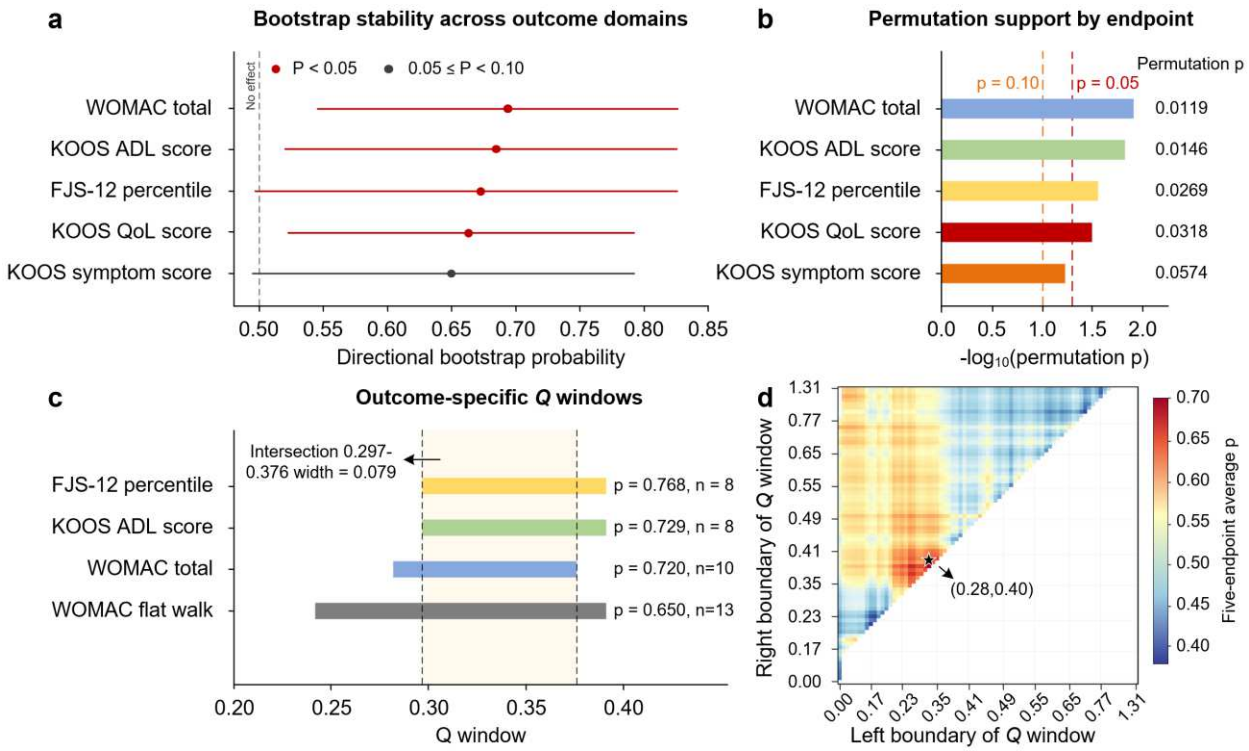
Beijing Postdoctoral Research Funding Program (DL)



Extended Data Fig. 1 | *Q*-defined rollback boundaries remain stable across subsets, and adding posterior tibial slope increases classification performance for the strict medial-pivot phenotype.

a, Estimated Q thresholds for the $R = 0$ and $R = 1$ boundaries in the all-knee, stable, and high-confidence subsets. The all-knee cohort included all knees with valid case-level Q and R measurements ($n = 131$). The stable-basin subset included knees whose path-level R values all remained within a single rollback phase region without crossing $R = 0$ or $R = 1$ ($n = 85$). The high-confidence subset included stable-basin knees with a path-level phase-angle range of $\Delta\Phi \leq 0.15$ radians ($n = 56$). Points indicate the mean estimated threshold, and horizontal bars indicate 95% confidence interval across repeated cross-validation analyses. Numerical labels

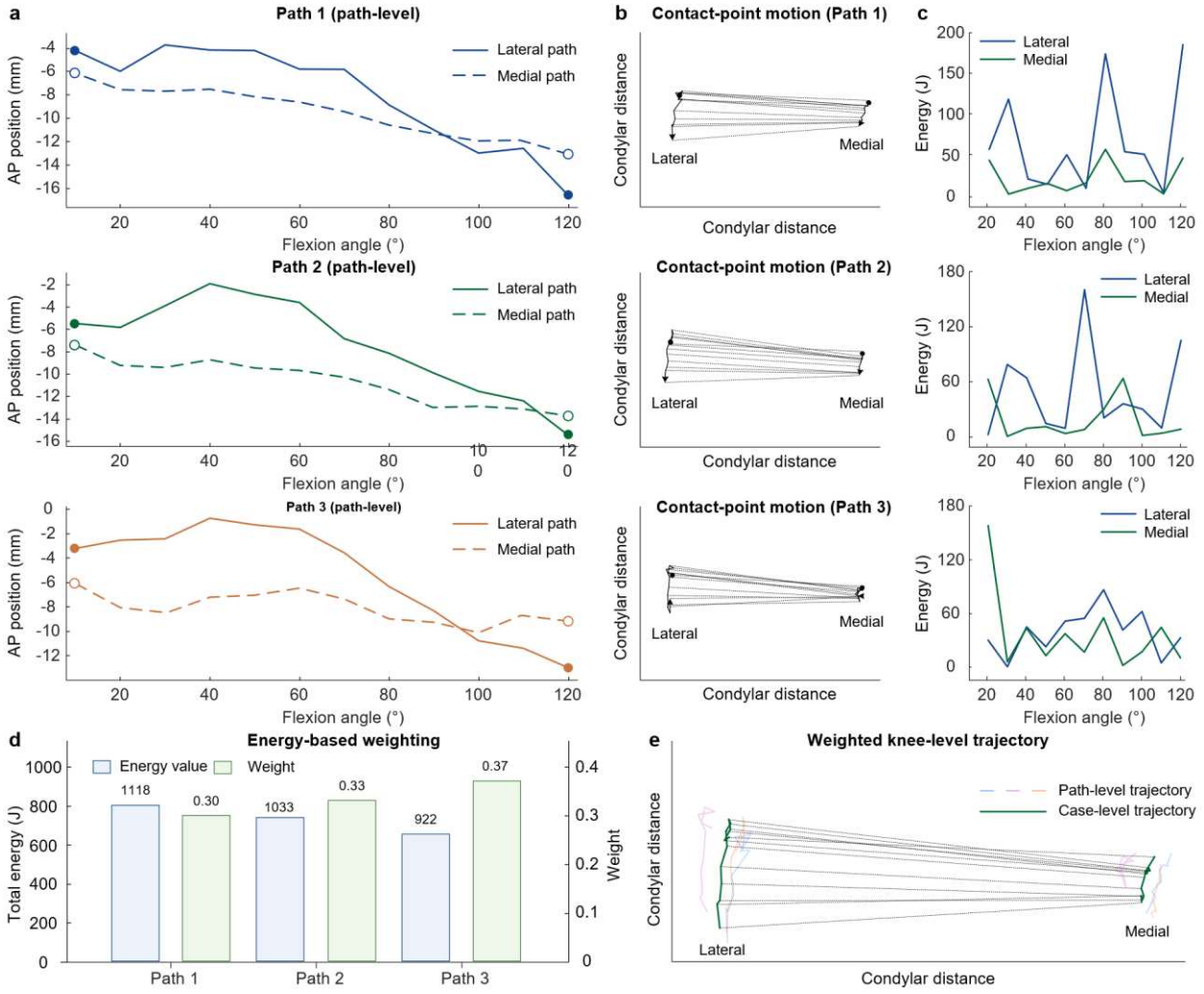
show the mean threshold estimates. The vertical dashed lines indicate the corresponding reference thresholds from the all-knee analysis. **b**, Endpoint sweep for defining the strict medial-pivot phenotype as $R > c$. The blue curve shows MBA across candidate values of c, and the gray curve shows the number of knees meeting the corresponding positive-class definition. The left vertical axis indicates MBA, and the right vertical axis indicates positive-class sample size. **c**, Knee-level consistency of Q-defined phase assignments across recorded kinematic paths. Bars show the numbers of knees whose paths remained within a single-phase region, crossed only the internal $R = 1$ boundary, crossed the lower boundary, crossed the upper boundary, or crossed both external boundaries. **d**, Classification performance for the strict medial-pivot phenotype ($R > 1.5$) using Q-only and Q-plus-slope models within the $Q \approx 0.35$–0.45 transition band.



Extended Data Fig. 2 | Resampling analyses support a stable outcome-derived *Q* window across postoperative outcome domains.

a, Directional bootstrap probabilities for postoperative outcomes comparing knees with *Q* values within versus outside each candidate window. Points indicate the estimated directional bootstrap probabilities, and horizontal lines indicate 95% bootstrap confidence intervals. The vertical dashed line at 0.50 indicates no directional preference. Red points denote endpoints with nominal $P < 0.05$ in the original between-group comparison, and dark-gray points denote endpoints with $0.05 \leq P < 0.10$. **b**, Permutation-test results for the five postoperative endpoints. Bar length represents $-\log10(P)$, and the numerical labels report the corresponding permutation *P* values. The orange and red vertical dashed lines indicate $P = 0.10$ and $P = 0.05$, respectively. Bar colors identify the corresponding outcome endpoints. **c**, Outcome-specific *Q* windows for endpoints meeting the prespecified resampling criteria. Each horizontal bar extends from the lower to the upper boundary of the corresponding window. The shaded region indicates the common

intersection of the four windows, spanning $Q = 0.297–0.376$. Numerical labels report DBP and the number of knees within each window. Colors correspond to the outcome endpoints shown in b. **d**, Exhaustive two-boundary search across candidate Q windows. The horizontal and vertical axes indicate the lower and upper window boundaries, respectively. Color represents the mean directional bootstrap probability across the five postoperative endpoints. Only boundary pairs for which the lower boundary was smaller than the upper boundary are displayed. The star marks the selected outcome-derived window of $Q = 0.28–0.40$.



Extended Data Fig. 3 | Energy-based weighting integrates repeated path-level kinematics into a knee-level trajectory.

a, Three repeated path-level kinematic recordings from one representative knee. Each row shows one flexion path. Solid lines indicate the lateral AP contact-point position, and dashed lines indicate the medial AP contact-point position across flexion angles. Filled and open circles mark the terminal lateral and medial contact-point positions, respectively. **b**, Two-dimensional representations of contact-point motion for the three recorded paths. Each gray line connects the lateral and medial contact points at one flexion angle, and the black traces connect sequential contact-point positions within each compartment. **c**, Lateral and medial trajectory-energy profiles

for the three paths. Energy values were calculated at each flexion angle using the corresponding compartmental trajectory and stiffness data according to the energy formulation described in the Methods. Blue and green lines indicate the lateral and medial energy components, respectively. **d**, Total trajectory energy and normalized path weight for each recording. Light-blue bars indicate the total path energy, and light-green bars indicate the corresponding normalized weight. Numerical labels above the bars report the total energy and weight for each path. **e**, Energy-weighted knee-level trajectory calculated from the three path-level trajectories. Light-colored traces indicate the individual path-level trajectories, and the dark-green trace indicates the weighted knee-level trajectory. At each flexion angle, the knee-level contact-point position was calculated as the weighted sum of the corresponding path-level positions using the weights shown in **d**.

Supplementary Files

This is a list of supplementary files associated with this preprint. Click to download.

- SupplementaryMethods.pdf